Composites Part B 215 (2021) 108799

Contents lists available at ScienceDirect

Composites Part B

journal homepage: www.elsevier.com/locate/compositesb

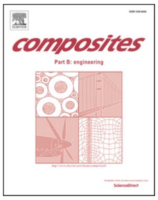

Anomalous Si-based composite anode design by densification and coating strategies for practical applications in Li-ion batteries

Moon Kyu Cho [a], Seung Jae You [a], Jung Gyu Woo [a], Jung-Chul An [a], Sujin Kang [b], Hyun-Wook Lee [b], Ji Hoon Kim [c], Cheol-Min Yang [c,*], Yong Jung Kim [a,**]

[a] Research Center for Secondary-Battery Materials, Research Institute of Industrial Science & Technology (RIST), Pohang-shi, 37673, Republic of Korea
[b] School of Energy and Chemical Engineering, Ulsan National Institute of Science and Technology (UNIST), Ulsan, 44919, Republic of Korea
[c] Institute of Advanced Composite Materials, Korea Institute of Science and Technology (KIST), Wanju-gun, Jeollabuk-do, 55324, Republic of Korea

ARTICLE INFO

Keywords:
Li-ion battery
Silicon-based anode
Highly densified anode
CVD coating
Binder pitch

ABSTRACT

Si-based Li-ion battery (LIB) anode materials often possess porous structures to accommodate the intrinsic volumetric expansion of Si upon cycling. However, the porous structure may cause poor initial coulombic efficiency (ICE), inadequate cycle life due to the continuous generation of a solid-electrolyte interface, and incompatibility with calendaring processes. To overcome these issues, we designed an optimized Si/C (*P*–Si/C) composite anode consisting of Si nanoparticles, graphite, and pitch, with a highly densified structure, suppressing Si expansion and enabling compatibility with the calendaring process. To further enhance the cycle life, the surface of the *P*–Si/C composite was modified by chemical vapor deposition using CH_4 gas (*C*–Si/C). The *P*–Si/C anode exhibited a high ICE of 88.0% with a rapid surge up to 99.0% after only the 4th cycle. The *C*–Si/C anode presented an improved capacity retention of 49.5% after the 39th cycle, compared with 46.0% for the *P*–Si/C anode after the 31st cycle, while maintaining the same ICE. Moreover, anodes prepared with 8 wt% *P*–Si/C or *C*–Si/C and 92 wt% graphite (*m-P*-Si/C and *m-C*-Si/C, respectively) showed higher capacity retentions compared with pure Si/C anodes. The *m-C*-Si/C anode exhibited a higher capacity retention of 80.1% after the 40th cycle, compared with 71.2% for the *m-P*-Si/C anode. The *m-C*-Si/C anode also displayed an extremely low expansion rate and the majority of the expansion was elastically recovered. This *C*–Si/C composite provided a controllable means to modify the performance of LIBs by simple mixing with graphite.

1. Introduction

Presently, Li-ion batteries (LIBs) are considered indispensable power storage devices for portable electronics, electric vehicles (EVs), and energy storage systems [1–3]. However, contemporary LIBs need further improvement in terms of energy density and stability. For instance, batteries mounted on EVs require an extended driving range, i.e., a higher energy density, to be comparable to traditional vehicles powered by internal combustion engines. Graphite is the most common anode material employed in commercial LIBs owing to its low electrochemical reaction potential and good cycle stability. However, its relatively poor hosting capability for Li ions (355–360 mAh g^{-1}) is a significant drawback. Therefore, metals forming compounds upon lithiation, such as Si, Sn, Ge etc., have replaced graphite as next-generation anode materials for LIBs. Among them, Si shows the highest theoretical capacities of 4200 mAh g^{-1} and 3579 mAh g^{-1} for $Li_{22}Si_5$ and $Li_{15}Si_4$, respectively, at ambient temperatures [4–7]. Furthermore, Si anodes exhibit a diverse range of merits, including a moderate working potential (~0.4 V vs. Li/Li^+), low cost, abundant availability, and environmental friendliness. However, similar to other metallic candidates, Si suffers from enormous volume expansion. During volume expansion/contraction with repetitive charge/discharge, cracking-induced pulverization of Si causes rapid capacity fading owing to its detachment and electrical isolation in electrode structures. Therefore, various engineering strategies have been developed to alleviate stress induced by volume changes, using a variety of nanomaterials and their composites with carbon materials, such as graphite, pitch, and tar [8–16].

The strategies for using Si as the LIB anode material include 1) Si/SiO_x and other alloys with a buffering domain for volume expansion (active/non-active mixed-phase), 2) porous or non-porous Si with a buffer space for accommodating volume expansion, and 3) nano-

---

* Corresponding author.
** Corresponding author.
E-mail addresses: cmyang1119@kist.re.kr (C.-M. Yang), ykimj@rist.re.kr (Y.J. Kim).

https://doi.org/10.1016/j.compositesb.2021.108799
Received 21 November 2020; Received in revised form 17 February 2021; Accepted 13 March 2021

Nomenclature and abbreviations

BET	Brunauer–Emmett–Teller
CB	Carbon black
CC mode	Constant-current mode
CC-CV mode	Constant-current-constant-voltage mode
CMC	Carboxy methyl cellulose
C–Si/C	CVD-treated silicon/carbon composite
CVD	Chemical vapor deposition
DEC	Diethyl carbonate
DFT	Density functional theory
EC	Ethylene carbonate
EDS	Energy-dispersive X-ray spectroscopy
FESEM	Field-emission scanning electron microscopy
FWHM	Full width at half maximum
EMC	Ethyl methyl carbonate
EVs	Electric vehicles
FEC	Fluoroethylene carbonate
FIB	Focused ion beam
H–Si/C	Heat-treated silicon/carbon composite in argon atmosphere
ICE	Initial coulombic efficiency
LIBs	Lithium-ion batteries
m-C-Si/C	CVD-treated silicon/carbon composite (8 wt%) mixed with graphite (92 wt%)
m-C-Si/C(10)	CVD-treated silicon/carbon composite (10 wt%) mixed with graphite (90 wt%)
N/P ratio	Areal capacity ratio of negative to positive electrode
PSDs	Particle size distributions
m-P-Si/C	Pristine silicon/carbon composite (8 wt%) mixed with graphite (92 wt%)
P–Si/C	Pristine silicon/carbon composite
PVDF	Polyvinylidene fluoride
SEI	Solid-electrolyte interface
SBR	Styrene butadiene rubber
Si/C	Silicon/carbon composite
SiNPs	Silicon nanoparticles
SSA	Specific surface area
TEM	Transmission electron microscopy
XRD	X-ray diffraction

engineered Si/C composite materials with tube, particle, and wire designs. Among them, SiO_x has received considerable attention from the battery industry owing to its relatively low volume expansion rate of ~160% and high capacity of 3172 mAh g^{-1} ($Li_{5.22}SiO$) when Li_2O becomes dominant over Li-silicates [17,18]. However, the intrinsic low initial coulombic efficiency (ICE) of SiO_x limits the amount that can be added to the graphitic anode material in LIBs (i.e., below 4 wt%). On the contrary, greater amounts of the Si/C composite material can be added compared with SiO_x owing to its higher ICE. Therefore, Si/C composite materials are preferable to SiO_x composites as anode materials for next-generation commercial LIB systems with capacities of 500–600 mAh g^{-1}.

The collapse of Si particles can be mitigated by reducing the particle size, and the volumetric change during charge/discharge cycles can be accommodated by the porous structure of Si and its composites. However, the exposure of a large surface area to electrolytes facilitates the build-up of a solid–electrolyte interface (SEI) caused by side reactions, lowering the ICE and electrode density, and thereby adversely affecting battery characteristics [12,19]. Strictly speaking, to address the volume expansion of Si particles, a buffer space is required; however, this space adversely affects the performance of the battery, resulting in loss of volumetric energy density and ICE. Si exhibits approximately a 10 times higher gravimetric capacity than graphite, however, its volumetric capacity does not differ as drastically. Owing to the considerable expansion of Si, the volumetric capacity difference between graphite and Si decreases drastically compared with the difference in gravimetric capacity. The actual volumetric capacities of Si and graphite after intrinsic expansion correction are recalculated as 2223.8 and 754.2 mAh cc^{-1}, respectively. These theoretical values are based on the ideal expansion ratio of each material (i.e., 4.4 times for Si and 1.1 times for graphite) upon cycling. The adjusted ratio of volumetric capacity difference between the two materials can be reduced to 2.95 times, much smaller than the gap in gravimetric capacity (i.e., 11.29 times). Therefore, suppressing the expansion rates of Si and graphite is essential in terms of energy density. Furthermore, void space, accommodating Si expansion, is not compatible with the calendaring process in standard cell fabrication [20]. To suppress the swelling rate of Si-based anodes during repetitive cycling, graphite and pitch were used as a ductile matrix and binder, respectively. This effectively holds the Si nanoparticles (SiNPs) together, thereby accommodating Si volume expansion upon cycling and providing high electrical conductivity with structural stability. Piper et al. have discussed the advantage of incorporating external compressive stress on Si-based anode materials [21–24]. Mechanical confinement of the Si particles in the carbonaceous matrix was helpful in maintaining electrical contact and minimizing the pulverization of Si particles in the electrode during cycling. These reports demonstrated that encapsulation by robust matrix material suppresses the volumetric expansion and pulverization of Si particles upon lithiation. Furthermore, a carbon-coated layer could effectively protect the active materials from side reactions with electrolytes, resulting in enhanced cycle stability and coulombic efficiency of anode materials over repeated charge/discharge cycles [25–30].

As a key strategy for adapting Si to be an active material of a LIB anode, a hierarchical introduction of buffering intermediate space formed by a combination of Si–graphite and pitch was achieved by blending Si particles with graphite powder and/or carbonaceous materials at contents of up to 5 wt% [31,32]. This addresses the instability problem of Si. Previous studies investigated a Si–graphite composite using a scalable chemical vapor deposition (CVD) of SiH_4 gas on graphite powder [33,34]. A reversible capacity and ICE of 517 mAh g^{-1} and 92%, respectively, were obtained with a capacity retention of 96% at the 100th cycle by introducing a Si-nanolayer–embedded graphite/carbon hybrid. The pitch-coated layers significantly contributed to the capacity retention. However, the expensive manufacturing process for high-purity SiH_4 gas (6 N) and the uneven formation of Si nanolayers should be resolved before full commercialization.

In this study, we synthesized unique Si/C composite structures, wherein mixtures of SiNPs, graphite, and pitch were highly densified and CVD-treated to enhance the dimensional stability and cycle life of Si-based LIB anodes, respectively. The electrochemical performances of LIB anodes fabricated with pure Si/C composites or mixtures of Si/C composite and graphite were examined in both pristine and CVD-treated forms. The results showed the potential of the novel Si/C composite as a next-generation LIB anode material.

2. Experimental section

2.1. Materials and methods

2.1.1. Synthesis of Si/C composites

The preparation of the Si/C composites included four steps: powder mixing, spray drying, hot-pressing, and pulverization/sieving. Si/C composites were prepared by mixing carbon-coated SiNPs (~40 nm in diameter, Nanomakers, France, Fig. S1), graphite flakes (battery grade, POSCO Chemical, Korea), and pitch (Carbores P, Rütgers, Germany). Carbon-coated SiNPs were prepared using a laser ablation method. The SiNPs possess thin carbon-coated layers (~1 nm) on their peripheries due to the decomposition of C_2H_2 gas. Initially, 197.6 g of SiNPs and 114.4 g of graphite were mixed using a MECHANOFUSION® System (AMS-Lab, Hosokawa Micron Corp., Japan) by combining three-dimensional circulation, high-speed/high-frequency compression, and shear forces. This unique mixing method is important to prevent the embedding of SiNPs into the graphite lattice because lithiation of the embedded SiNPs leads to cracking of carbon materials. Next, the SiNP–graphite powder mixture was homogeneously dispersed in a gum arabic aqueous solution (16.2 g in 2030 mL distilled water) with 246.1 g of binder pitch. The mixed dispersion was subjected to a spray dryer with a disk-type atomizer using KL-8 (Seo Gang Engineering Co., Ltd., Korea) at 20000 rpm, a feed flow rate of 32 mL min^{-1}, an air inlet temperature of 220 °C, and an outlet temperature of under 92 °C. The powders were collected in a cyclone chamber, compressed up to 0.7 ton cm^{-2}, and maintained at 250 °C to remove the internal surface area of the particles. Because the softening point of the binder pitch is 250 °C, the press temperature was set to approximately 260 °C to sufficiently impregnate the pitch into the internal space by lowering its viscosity. The samples were then carbonized at temperatures up to 900 °C for 1 h with a step at 400 °C for 2 h and a ramp rate of 5 °C min^{-1}. The particle size was controlled by a pin mill and sieved with a mesh (number 635, 20 μm pore size). The final composition of the anode material after heat treatment was 39:38:23 (SiNPs:pitch:graphite) in terms of weight fraction. Post-heat- and CVD-treatments were performed in a horizontal tube furnace (Fig. S2). A 10 g sample was slowly heated to 1000 °C at a rate of 5 °C min^{-1} (*P*–Si/C) and maintained for 1 h in an Ar atmosphere, with a flow rate of 200 sccm (*H*–Si/C). Once the temperature reached 1000 °C, CH_4 was introduced at a flow rate of 400 sccm as a carbon feedstock (*C*–Si/C). To investigate the surface structure variation due to the atmosphere, samples treated in Ar and Ar/CH_4 were analyzed.

2.1.2. Characterization

Raman spectra and images were obtained by microfocus optics tests using a 50 × objective lens, a 532 nm laser excitation source, and a confocal imaging Raman microscope (Nanophoton Inc., Japan). Two-dimensional images were obtained by Raman mapping and consist of 125 pixels in the X–Y directions, corresponding to 400 nm in the excitation spot size. The laser power was set at 1.29 mW to avoid thermal shifts of Raman peaks and damage to the Si/C composite powder from local overheating. A 50 × 50 μm area was chosen for collection of spatial maps to determine the difference in Si exposure and relative carbon lattice structure. The spectrum was acquired in a single scan with an exposure time of 1 s. A two-dimensional image at each condition was taken after 4 h 27 min. The crystalline structures of the samples were confirmed using an X-ray diffractometer (Dmax 2500/PC, Rigaku Co., Japan) with two goniometer systems. The accelerating voltage and current were 40 kV and 200 mA, respectively. The particle size distributions (PSDs) of the products were measured using a particle size analyzer (CILAS1090, Cilas Co., France). A 0.025 g sample was added to 5 mL of isopropyl alcohol and dispersed for 30 s in an ultrasonic bath prior to the PSD measurement. The Brunauer–Emmett–Teller (BET) specific surface area (SSA), surface energy, and pore size distribution were determined using standard N_2 adsorption isotherms (77 K) on a 3-Flex surface area analyzer (Micromeritics, USA). The evaluations of the adsorption data based on a density functional theory (DFT) model were embedded in the software from Micromeritics and followed the theory of Ross and Oliver [17]. Electrical conductivity was measured using a 4-point probe type powder resistivity measurement system (HPRM-1000, Hantech, Korea) at a pressure range of 5–38 MPa. The weight of the inserted samples was fixed at 0.5 g. Overall sample morphology and surface topology were visualized using field-emission scanning electron microscopy (FESEM, Gemini SEM 500, Zeiss, Germany). Cs-corrected transmission electron microscopy (TEM, JEM-ARM200F, JEOL, Japan) and energy-dispersive X-ray spectroscopy (EDS, X-Max^{N}100TLE, UK) were used to confirm the presence of the CVD-derived carbon layers on the Si/C composite particles. The TEM specimens were prepared with thicknesses of 50–100 nm using focused ion beam (FIB, SIM3050SE, Seiko Instruments Inc., Japan) etching.

2.2. Electrochemical measurements

The working electrodes for the Si/C composite (*P*–Si/C, *H*–Si/C, and *C*–Si/C) alone were fabricated by mixing the Si/C composite as an active material, carbon black (CB, acetylene black, Denka Co., Ltd., Japan) as a conducting agent, and poly-acrylic acid as a binder in distilled water at a mass ratio of 75:1:24. The slurries were exhaustively mixed and cast onto a Cu foil with a thickness of 48–53 μm and dried at 120 °C for 30 min. Subsequently, the electrode sheets were calendared to increase the electrode density. The electrode densities of *P*–Si/C, *H*–Si/C, and *C*–Si/C were 1.01, 1.05, and 1.06 g cc^{-1}, respectively, and their loading amounts were 2.5, 2.8, and 2.7 mg cm^{-2}, respectively. The calendared electrodes were vacuum dried at 120 °C overnight. The electrochemical performances of the samples were characterized using a CR2032 coin-type half-cell, fabricated with Li metal, electrolyte, and separator. The electrolyte used was a 1 M $LiPF_6$ solution in a mixture of ethylene carbonate (EC) and ethyl methyl carbonate (EMC) (3:7 ratio, v/v), to which vinyl carbonate (1.5 wt%) and 1,3-propane sultone (0.5 wt%) were added. The assembled cells were characterized in the voltage range of 0.005–1.5 V at the first cycle with 0.1 C, and capacity retentions were characterized in the voltage range of 0.005–1.0 V from the second cycle with 0.5 C, performed using the battery testing system (TOSCAT-3000, Toyo Systems, Japan).

The working electrodes consisted of 8 wt% *P*–Si/C or *C*–Si/C composite mixed with 92 wt% graphite (*m*-*P*-Si/C and *m*-*C*-Si/C, respectively) and were fabricated by mixing the *m*-*P*-Si/C or *m*-*C*-Si/C as an active material, CB as a conducting agent, and carboxy methyl cellulose (CMC) with styrene butadiene rubber (SBR) as a binder in distilled water at a mass ratio of 95.8:1:1.7:1.5. The relative amounts of Si/C composite and graphite were adjusted to obtain an equivalent capacity of 430 mAh g^{-1}. The slurries were exhaustively mixed and loaded onto Cu foil that was 56–58 μm in thickness, followed by drying at 120 °C for 30 min. Then, electrode sheets were calendared to increase the electrode density. The electrode densities of *m*-*P*-Si/C and *m*-*C*-Si/C were 1.65 and 1.56 g cc^{-1}, respectively, and their loading amounts were 4.3 and 5.2 mg cm^{-2}, respectively. Electrochemical performances were characterized using a CR2032 coin-type half-cell, fabricated with Li metal, electrolyte, and separator. The electrolyte used was a 1 M $LiPF_6$ solution in a mixture of EC and diethyl carbonate (DEC) (1:1 ratio, v/v). The assembled cells were characterized in the voltage range of 0.005–1.5 V at the first cycle with 0.1 C, and capacity retentions were characterized in the voltage range of 0.005–1.0 V from the second cycle with 0.5 C.

The expansion ratios of the electrode sheets were measured using a micrometer after de-capping the coin cells in the charged state. To evaluate the capacity retention performance in a real cell, a pouch-type full-cell was prepared with high mass loading and tested up to the 300th cycle (Table S1). A conventional NCM622 ($LiNi_{0.6}Co_{0.2}Mn_{0.2}O_2$) cathode material was used and was slurry cast on an Al current collector with CB as a conducting agent and polyvinylidene fluoride (PVDF) as a binder in a mass ratio of 94:3:3. The mass loading level of the cathode excluding the weight of Al current collector was 14.61 mg cm^{-2}, and it was pressed to adjust its density. The electrode thickness was measured to be 98 μm excluding the Al current collector (15 μm). The areal capacity of the cathode was adjusted to 4.45 mAh cm^{-2}. To examine its performance, *C*–Si/C (10 wt%) mixed with graphite (90 wt%) (*m*-*C*-Si/C (10)) was used in a full-cell configuration. The mass loading level of the anode excluding the weight of Cu current collector was 6.36 mg cm^{-2}, and it was pressed to adjust its density as well. The electrode thickness was measured to be 78 μm excluding the Cu current collector (10 μm). The areal capacity of the *m*-*C*-Si/C (10) anode was adjusted to 5.40 mAh

cm^{-2}, designed with an areal capacity ratio of negative to positive electrode (N/P ratio) of 1.21. The *m-C*-Si/C (10) anode was fabricated by mixing the *m-C*-Si/C (10) as an active material, CB as a conducting agent, and CMC/SBR as a binder in distilled water at a mass ratio of 96.5:1.0:2.5 (1.0/1.5). A full-cell capacity of 1016 mAh g^{-1} was obtained at 0.1 C in constant-current (CC) mode. The electrolyte used was fluoroethylene carbonate (FEC, PuriEL) containing 1.0 M $LiPF_6$ with an EC:EMC ratio of 3:7 v/v. FEC (10 wt%) was added to the electrolyte to obtain a total electrolyte amount of 4 g. Prior to the electrochemical evaluation of the full-cell and to stabilize the surface potential of the electrode, aging was performed in constant-current mode at 0.1 C, 3.7 V, and with a cut-off at 25 °C. The full-cell was continuously charged in the constant-current-constant-voltage (CC-CV) mode at 0.1 C, 4.2 V, and with a cut-off at 2% of 1 Ah. The full-cell was discharged to 3.0 V and cut-off at 0.1 C. After aging, the gas evolved in the cell was removed using a vacuum pump. After a formation cycle, the full-cell capacity was confirmed in the CC-CV mode at 0.2 C, 4.2 V, with a cut-off at 2% of 1 Ah in the charging step, and the CC mode at 0.1 C with a cut-off voltage of 3.0 V in the discharging step. The capacity retention of the full-cell was evaluated in the voltage range of 3.0–4.2 V at charge and discharge rates of 0.5 C. The capacity value was averaged from measurements performed in triplicate. A full-cell test also was performed using a battery cycler (TOSCAT-3000, Toyo Systems, Japan) at 25 °C.

2.3. Side-view operando optical microscopy analysis

Side-view operando optical microscopy analysis of micron-sized pure Si and *C*–Si/C composite anodes was carried out using an Olympus BX53M optical microscope. A three-electrode cell (EC-CELL, ECC-Opto-SBS) was used: the *C*–Si/C composite anode was used as the working electrode and metallic Li as the counter and reference electrodes, along with a glass-fiber filter separator (GFF, EC-CELL, 600 mm). This cell was assembled in an Ar-filled glovebox. The electrolyte used was 1.3 M $LiPF_6$ in EC/DEC (3:7 v/v) with 10 wt% FEC. The fabricated cells were galvanostatically cycled using a BioLogic SP-200 potentiostat (BioLogic, France) at a current density of 0.5 mA cm^{-2}, a voltage of 10 mV, and maintained for 10 h to ensure complete reaction and thermodynamic equilibrium.

3. Results and discussion

3.1. Optimizing the fabrication and composition of highly densified Si/C composites

SiNPs approximately 40 nm in size were used to prepare the Si/C composites employed in this study (Fig. S1a and b). X-ray diffraction (XRD) patterns confirmed the crystalline structure of the SiNPs, and a crystallite size of 19 nm was calculated from the (111) facet (Table S2). The thickness of the deposited carbon layers is in the 1–3 nm range, formed on the periphery of SiNPs through continuous pyrolysis of C_2H_2 gas during synthesis (Fig. S1a and Table S2). Previous studies reported that carbon layers formed by CVD treatment of Si surfaces improve the electrical characteristics and form a benign SEI composition [35–37]. The electrochemical performance of the pure SiNP anode was measured in a coin-type half-cell fabricated with Li metal (Fig. S1c). The pure SiNP anode exhibited specific capacities of 4145 and 2500 mAh g^{-1} in charge and discharge modes, respectively (ICE of 60%). The initial discharge capacity rapidly decreased to less than 10% (320 mAh g^{-1}) until the 10th cycle and was constant up to the 50th cycle. The Si morphology did not catastrophically collapse until the 50th cycle. Although the initial efficiency of SiNPs is relatively lower than those of conventional SiNPs (Fig. S1d), SiNPs were selected as the Si source in this study because of their excellent dispersibility in water (required for solution preparation during the spray drying process) and their good electrical conductivity due to the carbon layers on their surface.

Fig. 1a shows a schematic illustration of the synthetic process for Si/C composites. To optimize the manufacturing conditions of the Si/C composites, structural changes upon varying the SiNPs, graphite, and pitch concentrations were first examined. Because the Si/C composite was used as an additive material with graphite rather than as a standalone, a material designed for a higher capacity is preferred. We therefore set the mixing composition of graphite and pitch to achieve a capacity of ~1300 mAh g^{-1}. According to a simple calculation using the theoretical capacities of graphite and pitch-derived carbon, i.e., 360 mAh g^{-1} and 250 mAh g^{-1}, respectively, the required SiNPs content was estimated to be at least 40 wt%. Therefore, the content of SiNPs was fixed at 40 wt%, and the optimal compositions of the pitch and graphite were selected after examining samples prepared with varying

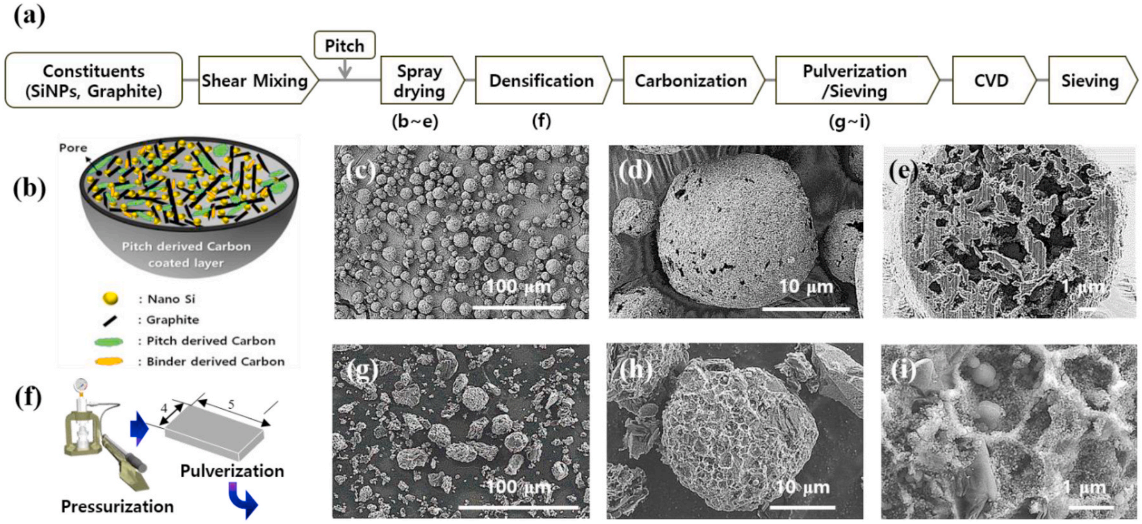

Fig. 1. Manufacturing process for Si/C composites and their morphological features after (c–e) spray drying and (g–i) densification/pulverization processes. (a) Flow chart for Si/C composite preparation. (b) Schematic illustration of Si/C composite spherules obtained by the spray drying process. The coating layer can be added or expelled as necessary. (c) FESEM image of the overall morphology of spray-dried Si/C composite spherules at low magnification (× 1000). (d) Magnified and (e) cross-sectional FESEM images of single spray-dried Si/C composite spherules (× 10000). (f) Schematic illustration of the densification and the dimensions of resultant Si/C composite blocks. (g) FESEM image of the overall morphology of densified and pulverized Si/C composite particles at low magnification (× 1000). (h, i) Magnified FESEM images of a single densified and pulverized Si/C composite particle (× 10000).

concentrations of them. The yields of pitch and gum arabic at 900 °C are 78% and 15%, respectively, which were also considered in material design. Fig. 1 also shows the morphologies of the products from the intermediate steps, including Si/C composite spherules after spray drying (b–e) and densification/pulverization processes (g–i). Fig. 1c–e shows the overall morphology at a low magnification (× 1000), surface morphology of a single spherule (× 10000), and cross-section obtained by FIB sputtering. Spherule manufacturing by spray drying was carried out to promote a homogeneous dispersion and to maintain good contact among all the components using the coagulation phenomenon. The prepared spherules possess a porous structure showing well-mixed graphite, SiNPs, pitch, and polymeric binder materials. In contrast to conventional Si-based electrodes, a porous structure can accommodate the stress caused by repetitive expansion and contraction. However, porous Si/C composite spherules were pressed to reduce their SSA and to suppress displacement due to expansion. Fig. 1f depicts the densification and dimensions of the molded Si/C composite block. The coated-carbon layers facilitate the formation of stable SEI layers by preventing chemical side reactions with the electrolyte. Hence, CVD treatment was carried out on the carbonized Si/C composite sample, whose particle size was controlled by sieving with a mesh screen. The CVD equipment, temperature profile, and yields at various conditions are shown in Fig. S2. Amorphous carbon generated from the decomposition of CH_4 feedstock was deposited on the surface of the *P*–Si/C composite causing a weight increase of approximately 6.0 wt%. Upon isothermal heat treatment for 1 h at 1000 °C in an Ar atmosphere without a CH_4 supply, the weight decreased by approximately 0.6 wt%. Thus, we concluded that the yield obtained by CVD treatment in a CH_4/Ar mixed gas is 6.6 wt%, considering the effects of the pyrolysis of pitch-derived carbon, Si/C composite, and deposition of CH_4 (Fig. S2c). Similar PSDs for Si/C composites were observed before and after CVD treatment, as shown in Fig. S3 and Table S3.

The cross-sectional morphologies of the densified Si/C composite anodes at each ratio were examined after FIB-assisted preparation. Fig. 2a–e shows the prepared Si/C composite anodes fabricated with pitch concentrations of 10, 20, 30, 40, and 50 wt%, respectively. The Si/C composites containing higher pitch contents are denser (Fig. 2c–e), whereas the number of voids increases as the graphite content becomes predominant (Fig. 2a and b). In particular, the internal pore volume decreases remarkably when the pitch content exceeds 30 wt%, and the amount of the darker colored domain, regarded as pitch-derived carbon, also increases (Fig. 2c–e). Fig. 2f–h shows the changes in SSA and pore structure of the Si/C composites presented in Fig. 2a–e. The SSA variations in the spray-dried porous Si/C composite spherules (indicated as rectangles) and densified Si/C composites after pressurization/pulverization (indicated by circles) (Fig. 2f), N_2 adsorption isotherms (Fig. 2g), and pore size distributions (Fig. 2h) of the densified Si/C composites demonstrate that the SSA and pore volume of the Si/C composites decrease as the pitch content increases. The SSAs of the porous and densified Si/C composites deviate at 30 wt% pitch content. Consequently, the SSA reduces to half that of the spray-dried porous Si/C composite spherules containing 50 wt% pitch content. Because the SSA of the anode material is related to the formation of a SEI, decreasing the SSA is advantageous for obtaining superior electrochemical properties. However, if excessive pitch is added, the electrical resistance of the composite may increase. Therefore, a Si/C composite with a balanced graphite/pitch composition should be formulated.

3.2. *Characterization of highly densified Si/C and C–Si/C composites*

The fundamental characteristics of the powders subjected to pulverization/sieving after densifying Si/C composite spherules are presented in Table S4. As the pitch content increases from 10 to 50 wt%, the SSA decreases linearly, whereas the tap density increases after heat treatment. Fig. 3a–h shows the FESEM, TEM, and elemental mapping (C, O, and Si) images of cross-sections of the optimized Si/C composite anode (red diamond in Fig. 2f) consisting of 39 wt% SiNPs, 23 wt% graphite, and 38 wt% pitch. The optimized Si/C composite anode exhibited a smaller SSA (7.4 $m^2\ g^{-1}$, Table 1) than that of the non-optimized sample containing 40 wt% pitch (10 $m^2\ g^{-1}$, Table S4). The individual components were uniformly dispersed, and the internal structure showed that SiNPs were not agglomerated and evenly dispersed along with the pitch. The graphite component existed as a filler and played an important role in enhancing the electrical conductivity. The cross-sectional images of the optimized Si/C composite anode, shown in Fig. 3a–d and Fig. S4, were observed at the same place. The optimized Si/C composite anode manufactured by calendaring was etched by FIB from the surface, and the cross-sections are shown in Fig. S4. The relatively dark areas correspond to graphite and pitch-derived carbon, whereas the brighter areas are SiNPs.

Fig. 3i–n shows a diagram of the CVD equipment, cross-sectional images of the Si/C composite obtained by TEM, and the elemental distribution obtained by EDS to confirm the surface profile after CVD treatment (designated as *C*–Si/C). Choi et al. [38] coated solid-phase pitch on a Si/C composite and revealed that the performance improved. The thickness of the pitch layers with 5 wt% coating was

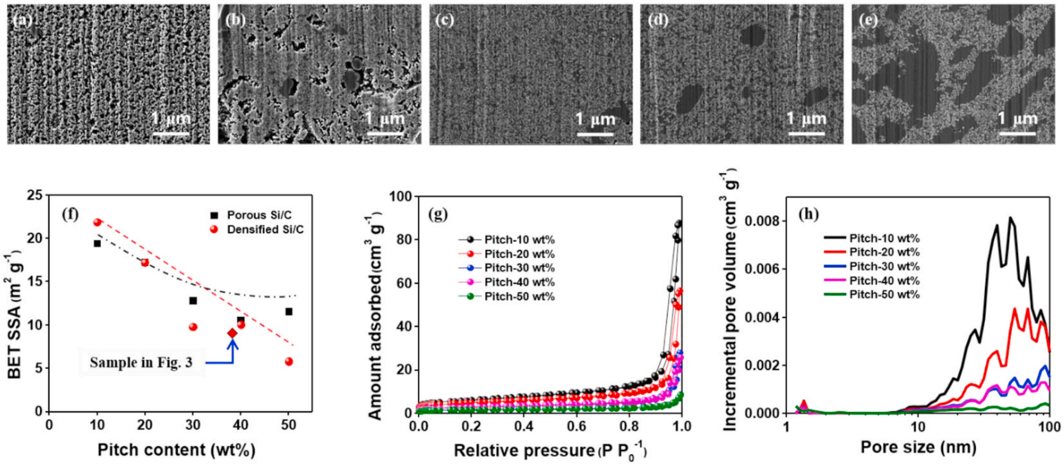

Fig. 2. Optimizing the processing of Si/C composite anodes for compositional control. (a–e) Cross-sectional FESEM images of the morphologies of Si/C composite anodes (pitch concentrations of 10, 20, 30, 40, and 50 wt%, respectively) with a fixed Si content at 40 wt% and a pitch/graphite ratio varied between 1/5 and 5/1. (f) SSA variation for porous Si/C composite spherules and densified Si/C composite particles as a function of the pitch content. (g) N_2 adsorption/desorption isotherms at 77 K and (h) pore size distributions (DFT method) for densified Si/C composite particle as a function of pitch content.

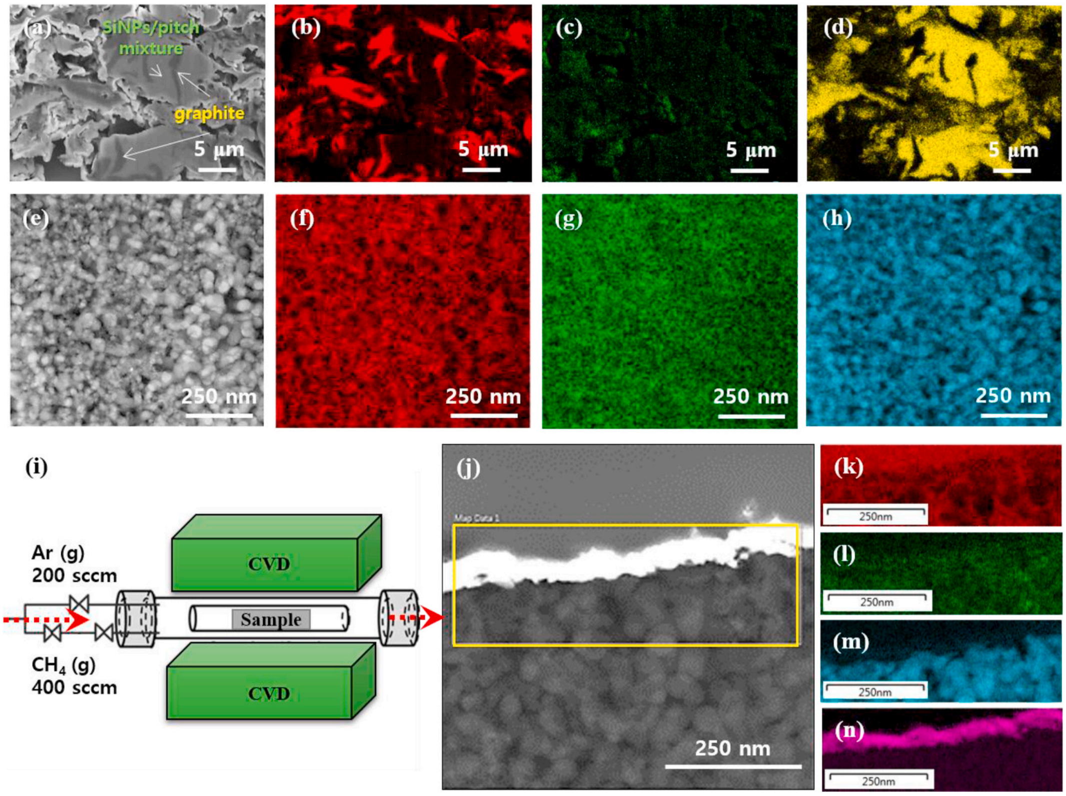

Fig. 3. FESEM and cross-sectional TEM images of the morphology of an optimized Si/C composite anode, indicated with an arrow in Fig. 2 (f). (a) Cross-sectional FESEM and (e) TEM images. Elemental mapping of (b, f) carbon, (c, g) oxygen, and (d, h) silicon. All the results are obtained from cross-sections of an electrode sheet prepared by FIB. (i) Schematic of the CVD equipment used. (j) Cross-sectional TEM image after CVD treatment of Si/C composite powder, which is the surface morphology observed in the FIB cross-section in Fig. S4. The deposited carbon-layer was not observed on the surface of the Si/C particle. The bright region is a Pt layer deposited to enhance the electrical conductivity of sample. (k–n) Elemental mapping images for the box indicated in part (j), showing the distributions of (k) carbon, (l) oxygen, (m) silicon, and (n) platinum. (For interpretation of the references to color in this figure legend, the reader is referred to the Web version of this article.)

Table 1
Pore structure parameters for Si/C composites depending on the post treatment.

Sample	BET SSA (m^2 g^{-1})	Total pore volume (cm^3 g^{-1})	Micropore volume (cm^3 g^{-1})	Micropore volume fraction (%)	Average pore size (nm)
P–Si/C	7.41	0.0114	0.0007	6.14	6.16
H–Si/C	6.77	0.0106	0.0006	5.66	6.26
C–Si/C	5.71	0.0099	0.0001	1.02	6.91

approximately 30 nm as observed by TEM. However, in our study, as shown in Fig. 3j–n, the carbon coating layer is not observed on the surface of the *C*–Si/C composite even though weight gain was confirmed in an Ar/CH$_4$ mixed gas atmosphere. Fig. 3j shows a cross-sectional image of the *C*–Si/C composite processed by FIB. The white layer is not a carbon coating layer, but a Pt layer (Fig. 3n) deposited to enhance the electrical conductivity of the sample, facilitating sample observation. Fig. 3k–n shows EDS maps of the area indicated by the yellow box in the TEM image (Fig. 3j), revealing the homogeneous distribution of C, O, Si, and Pt.

Fig. S5 shows the overall morphologies of particles in the *P*–Si/C (Fig. S5a–e), *H*–Si/C (Fig. S5f–j), and *C*–Si/C (Fig. S5k–o) composites, as observed by FESEM. Contrary to the trend observed for pitch [37], no significant difference is observed in the morphologies before and after the CVD treatment. However, subtle changes on the *C*–Si/C surface are observed at high magnification. SiNPs exposed between rugged grooves are not visible after CVD treatment, implying that surface voids and defects were filled with the deposited carbon layers. Not all particles display rough surfaces similar to pockmarks; some possess smooth surfaces, assumed to be graphite surfaces exposed by pulverization. However, *C*–Si/C seems to be coated with a foreign material, and interestingly, a similar surface morphology is observed in *H*–Si/C. It was difficult to clearly demonstrate structural differences using microscopic images. However, alternative analyses to determine the pore structures, surface energies, and electrical conductivities of the Si/C composite particles were performed to further understand the surface structure alteration induced by CVD treatment.

Fig. 4 shows the various particle properties in *P*–Si/C, *H*–Si/C, and *C*–Si/C composites. The pore size distributions (Fig. 4a), surface energies (Fig. 4b) determined from N$_2$ adsorption isotherms, and electrical conductivities measured using the 4-point probe method (Fig. 4c) were determined. From the pore size distribution analysis using DFT simulations, the pore volume significantly reduced after the CVD treatment over the entire range of pore sizes. Table 1 summarizes the pore characteristics after surface treatment. The initial SSA value of 7.4 m^2 g^{-1} decreases to 6.8 m^2 g^{-1} after heat treatment and further to 5.7 m^2 g^{-1} after CVD treatment, indicating the effectiveness of the CVD treatment in decreasing the SSA. The observed reduction of the SSA after heat treatment of *H*–Si/C is believed to be induced by the carbonization of pitch. Defects such as voids, cracks, and dislocations, can be removed by crystallization induced by heat treatment. A small SSA is thus advantageous in relation to the viscosity of the slurry, reducing binder consumption, and therefore reducing the amount of solvent required. As such, developments in the composition of various Si/C composites can provide a platform technology for Si-based LIB anodes with excellent electrical connectivity, mechanical robustness, and protection from side reactions. The surface energies before and after CVD treatment are

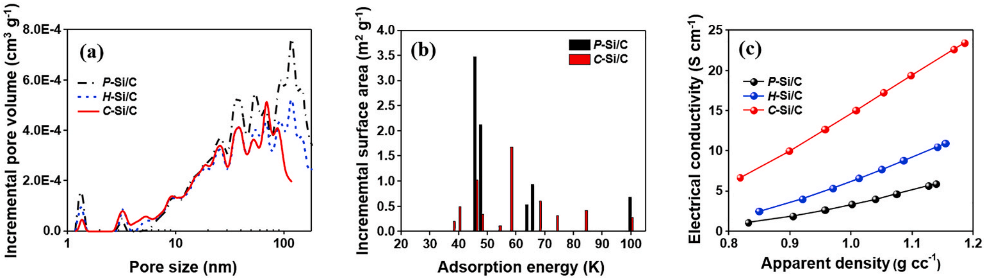

Fig. 4. Diverse physical properties of the optimized Si/C composite powders (*P*–Si/C, *H*–Si/C, and *C*–Si/C). (a) Pore size distributions, (b) adsorption energies obtained by the DFT method, and (c) electrical conductivities as a function of the apparent density, measured using the 4-point probe method at pressures between 5 and 40 MPa.

shown in Fig. 4b. The treated *C*–Si/C composite displays a complex surface energy distribution compared with that before CVD treatment, demonstrating that N_2 is adsorbed at different energies depending on the surface of the graphite crystallite. Previous studies have shown that the adsorption energy centered at approximately 50–60 K is generally attributed to the basal planes of graphite [39–41]. An adsorption energy below 50 K is related to the edge/prismatic plane, whereas energies above 60 K correspond to graphite defects. The peaks at 50–60 K that appear after CVD treatment indicate the thermal conversion of the pitch-based constituent to a more crystalline structure. Fig. 4c shows the electrical conductivities of Si/C composite powders. Because compression behavior depends on the properties of the powder, the electrical conductivities were compared in terms of apparent density to account for the structural changes due to compression. Each point was measured at the same pressure, and the structural variations as a function of the applied pressure were observed. The *H*–Si/C composite powder possesses a higher conductivity than *P*–Si/C as a result of the increased crystallinity upon heat treatment. The peaks observed in the XRD patterns of the *P*–Si/C, *H*–Si/C, and *C*–Si/C composites (Fig. S6) were well matched with those of crystalline Si (JCPDS card No. 27–1402). Importantly, peaks corresponding to SiC were not observed, indicating that the thermal treatment conditions were within a suitable range for suppressing carbide formation. Next, the crystallite sizes were calculated using the Scherrer equation (Fig. S6 and Table S5), demonstrating the effect of thermal treatment. A reduction in the full width at half maximum (FWHM) of the (002) peaks may be attributable to the crystallinity enhancement upon heat treatment. After the CVD treatment (*C*–Si/C), the FWHM value was slightly larger than that of *H*–Si/C. Therefore, the carbon layers introduced by the CVD treatment are presumed to possess low crystallinity, and its crystalline structure was analyzed by Raman mapping (Table 2). Fig. S7 shows the reconstruction of the results in Fig. 4c, considering pressure as the dominant parameter. *C*–Si/C exhibits the highest density compared with *P*–Si/C and *H*–Si/C at a high pressure (Fig. S7a). This result demonstrates that *C*–Si/C is more compressible than the other samples. The electrical conductivity values rapidly increase in the initial step of pressurization when the applied pressure is considered as an abscissa (Fig. S7b). However, a pseudo-linear or a slow initial step is observed when the apparent density of the powder is considered in Fig. 4c.

Fig. 5 represents the surface morphologies of the Si/C composite powders before (a–d) and after (e–h) CVD treatment obtained by Raman spectroscopy. Fig. 5a and e shows the images obtained at 500 × magnification. The indicated squares were analyzed using the XY mapping mode. The results obtained are shown in Fig. 5b, c, f, and g. The XY mapping mode was employed to measure the distribution of spectra in a plane, using point illumination. Fig. 5b and f shows the relative intensities of the peak at 520 cm^{-1} due to the exposed crystalline Si and the base line, and Fig. 5c and g shows the relative lattice structures of the coated carbon with respect to the intensity ratio of the D peak (~1350 cm^{-1}) to the G peak (~1580 cm^{-1}). These calculation methods are presented in Fig. S8. In Fig. 5b and f, the red colored areas in the spectrum correspond to a stronger Si crystalline peak. The CVD-derived carbon-coated Si/C surface prevents direct exposure of the Si surface to the electrolyte. In each spectrum, some Si particles are exposed even after CVD treatment; however, the relative ratio is small, and the intensity of the Si peak is low. In Fig. 5 c and g, the red color indicates a less-ordered carbon structure, demonstrating that a large amount of low-crystalline carbon (amorphous carbon) was introduced on the Si/C composite surface by CVD treatment. However, from FESEM images, it was difficult to confirm whether the carbon coating layers were formed on the Si/C composite. The *C*–Si/C composite exhibited a larger crystallite size than that of the *P*–Si/C composite but a smaller size than that of *H*–Si/C. Based on the Raman and XRD analyses, the deposition of carbon by CVD treatment filled and covered large irregularities only close to the surface of the Si/C particles. The deposited carbon smoothened the crater-like, rough surface (compare Fig. S5c and m), thereby altering SEI formation upon contact with the electrolyte. The surface features before and after CVD treatment are schematically shown in Fig. 7, and their effect will be discussed in more detail. Fig. 5d and h shows the averaged Raman spectra consisting of 15,625 pixels 400 nm in size. In general, the Raman results barely define the overall structure because of the limited size of the scanned area and the large deviations in each region. However, integration of the mapping results of the entire area makes it possible to obtain the average lattice structure. In Table 2, the characteristic parameters from the averaged Raman spectra before and after CVD treatment are summarized.

Table 2
Characteristic parameters obtained from Raman spectra of Si/C composites before and after CVD treatment.

Sample	Peak	Raman shift (cm^{-1})	Peak intensity	R (=I_D/I_G)
P–Si/C	D	1350	267	0.964
	G	1593	277	
C–Si/C	D	1353	156	0.987
	G	1593	158	

3.3. Electrochemical characterization of half-cells and pouch-type full-cells

To investigate the beneficial effects of the CVD treatment on LIB performance, the electrochemical properties of the pure Si/C composites (*P*–Si/C, *H*–Si/C, and *C*–Si/C) and their mixtures with graphite (*m*-*P*-Si/C and *m*-*C*-Si/C) were evaluated in half-cell configuration (Fig. 6). We summarized the initial charge/discharge profiles (Fig. 6a and e), the differential capacity (dQ/dV) profiles (Fig. 6b and f) in the first cycle, the capacity retentions (Fig. 6c and g), and the coulombic efficiencies (Fig. 6d and h). Table 3 shows the electrochemical properties of the pure Si/C composites and the Si/C mixtures with graphite. The coulombic efficiency of the *m*-*C*-Si/C composite anode is most stable at the 40th cycle (99.4%). The ICEs of all pure Si/C composite anodes are approximately 88%. The ICEs of the *m*-*P*-Si/C and *m*-*C*-Si/C composite anodes

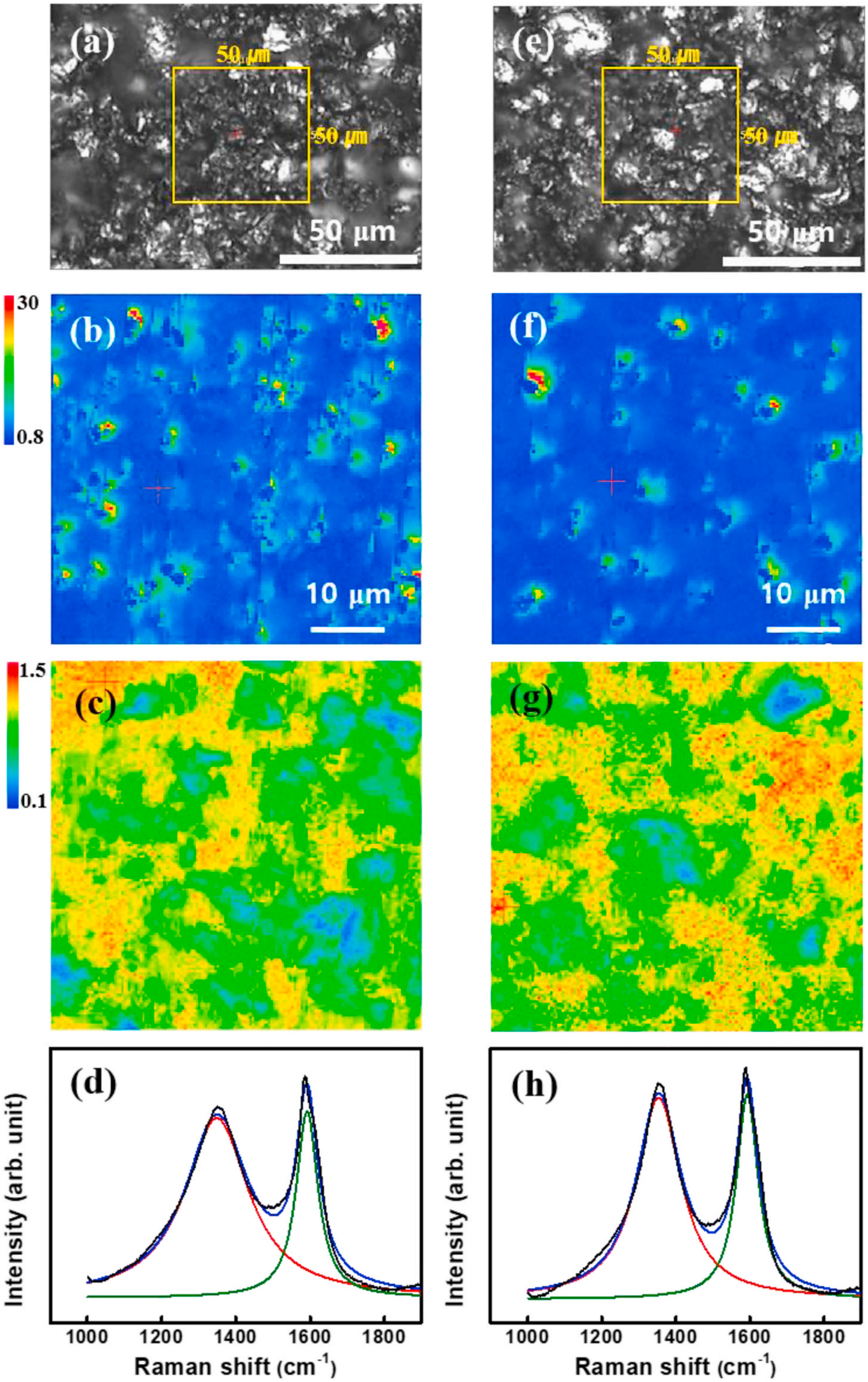

Fig. 5. Surface morphologies of the optimized Si/C composite powders (a–d) before and (e–g) after CVD treatment (*P*–Si/C and *C*–Si/C, respectively). (a, e) Optical microscopy images at 500 × magnification (ocular lens: 10 × , objective lens: 50 ×). The indicated squares were analyzed using the XY mapping mode. (b, f) Images obtained by Raman spectroscopy in mapping mode, based on the relative difference of the intensity of the peak at 520 cm^{-1} and the base line. (c, g) R values ($=I_D/I_G$) based on the intensity of the D and G peaks. (d, h) Averaged Raman spectra for the entire region of the mapping results, consisting of 15625 points. Each point implies an independent Raman measurement.

are 90.9% and 91.7%, respectively, indicating that CVD treatment is effective in enhancing the ICE. Consequently, the CVD treatment favorably affects SEI formation and cycle life. Fig. 6a shows the normalized first cycle of pure Si/C composite anodes (*P*–Si/C, *H*–Si/C, and *C*–Si/C). The profiles plotted with the specific capacity are shown in Fig. S9. The specific capacity values at the first cycle of pure Si/C composite anodes are 1459, 1382, and 1335 mAh g^{-1} for *P*–Si/C, *H*–Si/C, and *C*–Si/C, respectively. Despite a slight capacity loss after post-treatment (Fig. S9a), the normalized results show similar charge behaviors (de-lithiation). However, when the charging behavior is taken into consideration, the *P*–Si/C composite anode exhibits the lowest charging resistivity. The inset of Fig. 6a shows the discharge/charge behavior up to the 10th cycle. Fig. 6e compares the discharge/charge behavior of the mixture blended with the Si/C composite (8 wt%) and graphite (92 wt%). Compared with the results of the pure composite anodes, the mixtures presented opposite results in terms of resistive behavior during discharge at the first cycle owing to the differences in the extent of contact between the particles of the pure composite and mixtures with graphite. That is, the *C*–Si/C composite was more compressible than the non-treated samples. Considering the powder

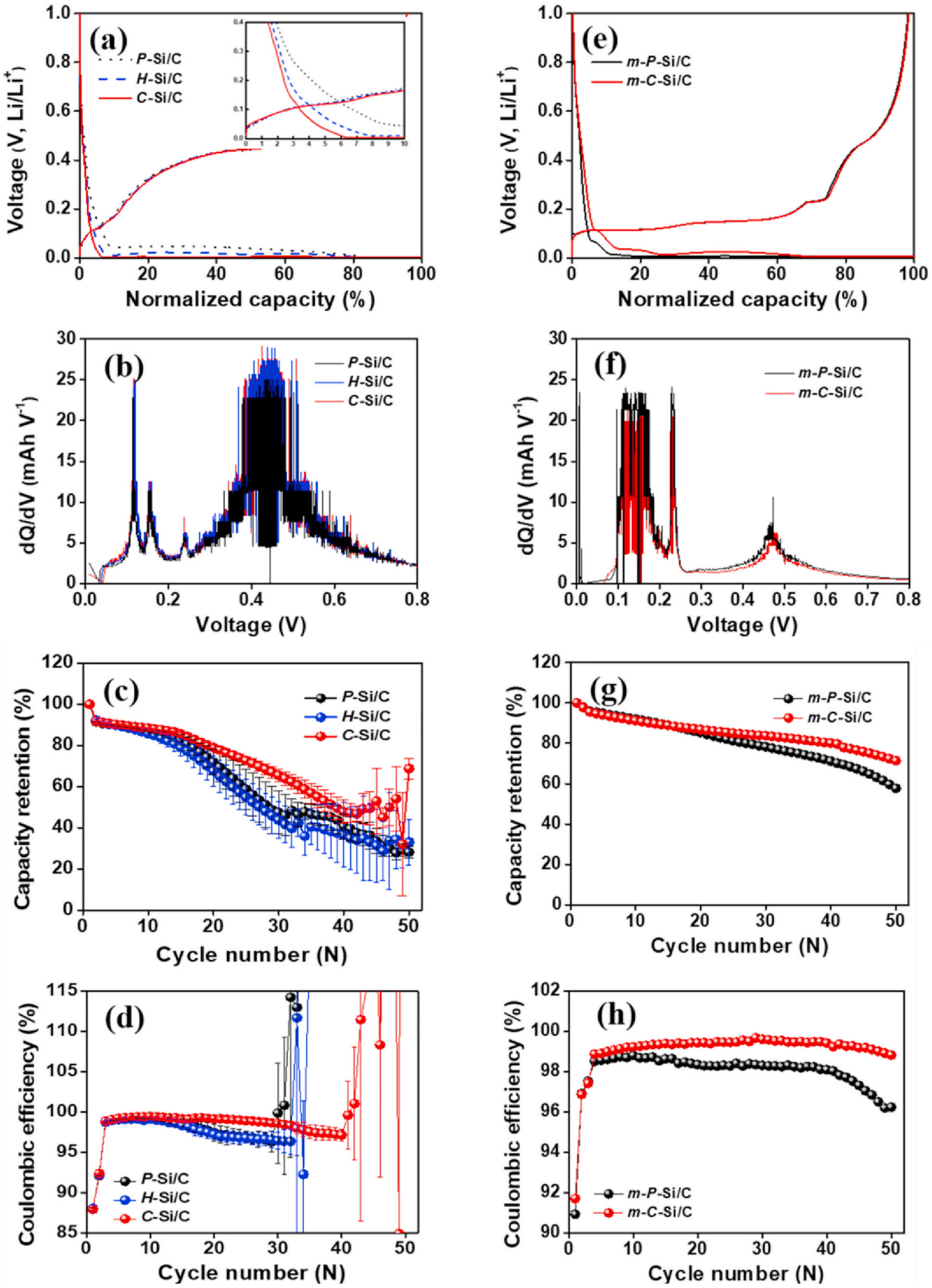

Fig. 6. Electrochemical performances of LIB anodes composed of (a–d) the optimized Si/C composite alone (*P*–Si/C, *H*–Si/C, and *C*–Si/C) and (e–h) the mixtures of 92 wt% graphite and 8 wt% Si/C composite (*m*-*P*-Si/C and *m*-*C*-Si/C) using a half-cell configuration. (a, e) Charge/discharge profiles, (b, f) differential capacity (dQ/dV) profiles of the first cycle, (c, g) capacity retentions, and (d, h) coulombic efficiencies.

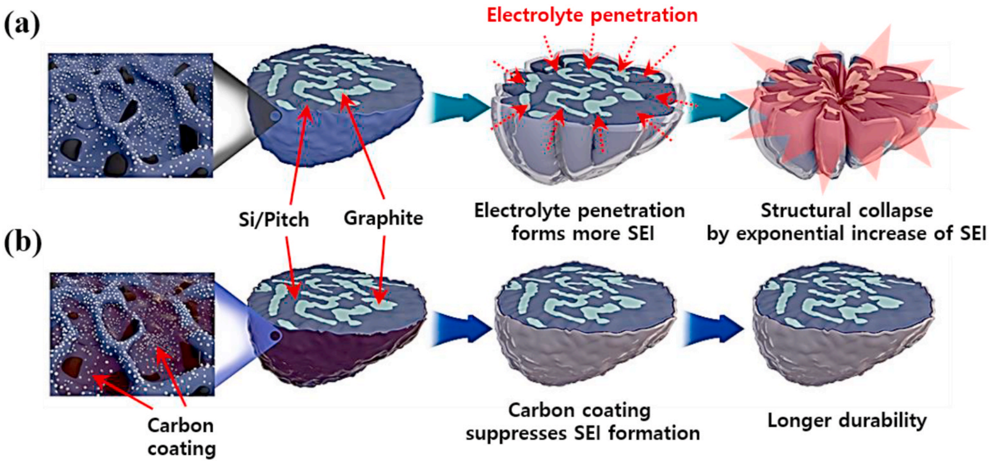

Fig. 7. Schematic models for the differences in structural robustness of (a) *P*–Si/C and (b) *C*–Si/C composites.

Table 3
Electrochemical properties of pure Si/C and Si/C/graphite composite anodes. The 8 wt% *P*–Si/C or *C*–Si/C composites were mixed with 92 wt% graphite (*m-P*-Si/C and *m-C*-Si/C, respectively).

Sample	Loading amount (mg cm^{-2})	Loading amount (mAh cm^{-2})	Electrode density (g cc^{-1})	Capacity @ 1st cycle (mAh g^{-1})				
				Charge	Discharge	1st cycle	30th cycle	40th cycle
P–Si/C	2.5	3.7	1.01	1655	1459	88.0	99.9	–
H–Si/C	2.8	3.9	1.05	1576	1382	88.1	96.5	–
C–Si/C	2.7	3.6	1.06	1520	1335	88.0	98.6	97.2
m-P-Si/C	4.3	1.9	1.65	487	442	90.9	98.3	98.1
m-C-Si/C	5.2	2.2	1.56	467	426	91.7	99.6	99.4

resistance variations with pressure, the density is presented in Fig. S7. The density of the *C*–Si/C varied from low to high values depending on pressure. The *C*–Si/C was well-pressed, inferring that the conductivity also increased rapidly with increased pressure. Therefore, the higher resistive behavior of *C*–Si/C in Fig. 6a is attributable to the malleability of the system caused by the carbon coating layer. That is, the malleability conferred excellent electrical conductivity. However, *m-C*-Si/C consisted of 92 wt% graphite; therefore, this composite was not easily compressible owing to the intrinsic elasticity of graphite (Fig. 6e), and the CVD-derived carbon beneficially affected the electrical conductivity. Therefore, the opposite tendency in charge profiles between the Si/C alone and the Si/C blended with graphite can be explained by the malleability of *C*–Si/C. It is presumed that *C*–Si/C, which deformed well under pressure, possessed more advantageous properties to improve the electrical conductivity with graphite. Fig. 6b and f presents dQ/dV *versus* voltage plots during discharge (lithiation). In Fig. 6b, the sharp peaks at 0.11, 0.15, and 0.24 V are attributed to the graphitic structure, whereas the broad peaks close to 0.47 V indicate Si de-alloying due to the desorption of Li ions during charging (de-lithiation). In relation to the peak intensities of the peaks at 0.46–0.47 V (i.e., characteristic of Si), the CVD-treated sample exhibited a slightly lower intensity (Fig. 6f) than the pristine sample. The peak intensity close to 0.46 V indicates the stability of the electrode. The small peak located at 0.46 V implies that *m-C*-Si/C possesses a higher resistance to deformation by repetitive discharge/charge cycles compared with *m-P*-Si/C. However, pure Si/C composite anodes showed an opposite trend in the mixture form. These characteristics also demonstrated the effect of structural difference depending on pressure, similar to the trend described in Fig. 6a and e. This characteristic peak for Si might affect the capacity retention and electrode swelling behavior. Fig. 6c and g shows the capacity retention characteristics up to 50 cycles for the pure Si/C composite and Si/C composite mixed with graphite. The *C*–Si/C composite anodes exhibited excellent capacity retention properties compared with the composites without CVD treatment in both pure and mixed Si/C composites. In Fig. 6c, the capacities of *P*–Si/C and *H*–Si/C composite anodes begin to deviate at approximately the 30th cycle. The *C*–Si/C composite anode exhibits an improved capacity retention of 49.5% after the 39th cycle, compared with 46.0% after the 31st cycle for the *P*–Si/C composite anode, while the same ICE is observed for both anodes. The drastic increase in error bars and deviations is attributed to structural collapse of the composite particles. The *C*–Si/C composite anode presents the best results in terms of capacity retention ratio without an abrupt change. In Fig. 6g, a similar trend for the capacity retention is observed, confirming that the capacity retention ratio of the *m-C*-Si/C composite anode (80.1%) is superior to that of the *m-P*-Si/C composite anode (71.2%) after the 40th cycle. The coulombic efficiencies measured for both types of anodes are presented in Fig. 6d and h. The *P*–Si/C composite anode exhibits a high ICE of 88.0% with a rapid surge up to 99.0% after only the 4th cycle (Fig. 6d). The *C*–Si/C composite displays the best performance. Comparing the coulombic efficiencies at the 30th and 40th cycles, as shown in Fig. 6d and Table S4, the *P*–Si/C composite anode begins to change abruptly from the 30th cycle. The *H*–Si/C composite anode also exhibits a rapid deviation in the 32nd cycle, implying that the internal collapse is initiated by Si species. Differences in the coulombic efficiencies may originate from the different SSA as the outermost surface of the powder was responsible for initial SEI formation. In liquid electrolytes, expansion and shrinkage of Si particles upon charge-discharge causes repetitive exposure of the fresh surface, resulting in unceasing formation and thickening of SEI layers. Therefore, the CVD-derived carbon on the Si/C composite might prevent direct contact between the exposed Si and the electrolyte solution, thereby suppressing excessive reactions that form the SEI. For the graphite-hybridized anode, the *m-C*-Si/C composite anode achieved an ICE of 91.7% and a coulombic efficiency of 99.0% in the 4th cycle, after which it maintained a coulombic efficiency of approximately 99.4% after the 40th cycle (Fig. 6h and Table 3). The *m-C*-Si/C composite anode also showed a capacity retention of 80.1% after the 40th cycle, superior to the *m-P*-Si/C composite anode (71.2%), as shown in Fig. 6g. Therefore, coating a carbon layer on the *P*–Si/C composite is effective to obtain high coulombic efficiency and cycle stability due to optimization of the surface structure.

Fig. 7 presents schematic models of the variations in the structure as distinguished by the presence of the carbon coating layer due to continuous SEI growth during repetitive cycling. As shown in Fig. 1i, the sample without a coating exhibited an extremely rough topology similar to moon craters, however, the sample with the carbon coating possessed a relatively smoother surface. Hence, we can explain why they differ in terms of electrochemical properties. For the sample without coating, the electrolyte can permeate into the internal structure through the rough surface topography (Fig. 7a). The SEI formed on the surface facing at an angle pushes each other as it grows, causing structural cracking on the periphery of the Si/C composite particles, and the SEI is reformed on the fresh surface of the cracks. Such crack propagation induces a catastrophic collapse of the entire morphology. On the contrary, carbon coating prevents electrolyte permeation and decreases the number of side reactions and SEI formation (Fig. 7b). The carbon coating layer can also improve the electrical conductivity of the entire particle.

To confirm the practical viability of the *C*–Si/C composite, electrochemical tests were carried out in a pouch-type full-cell configuration using an industrial electrode (see details in experimental section and Table S1). The test cell comprised a cathode (NCM 622) and an anode (*m-C*-Si/C (10)). The dimensions of the pouch-type full-cell are shown in Fig. 8a, i.e., 55.5 mm in height and 32 mm in width. The cycle retention properties were examined in CC mode at 0.5 C. As shown by the normalized capacity retention (Fig. 8b), the *m-C*-Si/C (10) composite anode displays excellent cycle retention properties, exceeding 82% at the 300th cycle. Owing to the low SSA due to the dense particle morphology and surface carbon coating, SEI evolution was well suppressed. Furthermore, carbon coating layers facilitated the compression of the *m-C*-Si/C (10) composite by graphite particles, providing excellent contact. The reduced SSA and excellent electrical connectivity of the *m-C*-Si/C (10) composite contributed to the greater stability of the Si-based anode.

Table S6 summarizes the expansion ratios of the anodes obtained in the lithiated states after 50 cycles using a coin-type half-cell. The volume expansion of the porous Si/C composite spherule at the 50th cycle is compared with that of the densified Si/C composites (*P*–Si/C, *H*–Si/C, and *C*–Si/C) obtained by pulverization of the compressed molding. The *C*–Si/C composite anode exhibits enhanced capacity retention upon repetitive charge/discharge cycling up to the 50th cycle; however, it presents a slightly larger swelling ratio than that of the *P*–Si/C composite anode. The porous Si/C composite spherules show the largest expansion ratio of 146.4%. The densified Si/C composite (*P*–Si/C, *H*–Si/C, and *C*–Si/C) anodes exhibit expansion ratios of 111.3–136.3% at the 50th cycle when they are applied as an anode. Notably, when the *P*–Si/C composite is mixed with graphite (*m-P*-Si/C), the expansion ratio drastically decreases to 63.8%. When the *C*–Si/C composite is mixed with graphite (*m-C*-Si/C), the expansion ratio decreases to 62.5%.

To clarify the effect of the densification step in the preparation of Si/C composite anodes, operando optical microscopy observations were performed. For comparison, a micron-sized pure Si (approximately 3 μm in size) anode was compared with the densified *C*–Si/C composite anode. Fig. 9a and b shows the expansion and contraction features of the micron-sized pure Si and *C*–Si/C composite anodes. For the pure Si anode, rapid expansion occurred during lithiation; however, the anode displacement was not recovered during de-lithiation. In contrast, in the *C*–Si/C composite anode, expansion during lithiation was recovered elastically during de-lithiation (Fig. 9c and d). The *C*–Si/C composite anode possessed sufficient bonding strength to withstand structural collapse caused by the expansion of Si and provided structural robustness that could be elastically recovered. The drastic difference between both cases is presented in the Movie file in supplementary data. It demonstrates that the densified Si/C composite anodes sufficiently accommodated the volume change in the high-density structure and that volume expansion upon charging could be elastically recovered.

4. Conclusion

Si, graphite, and carbon composites were fabricated to provide a practical LIB anode material with a high ICE and cycle retention performance. When Si was directly mixed with graphite, a local dead space may occur due to the loss of electrical contact with graphite, resulting in rapid deterioration of cycle performance. However, the preparation of an intermediate buffer medium for Si and its binary combination with graphite were determined to be incredibly effective in improving the efficiency, cycle life, and electrode dimensional stability while maintaining a high capacity similar to SiO_x. Furthermore, the ICE was improved to a satisfactory level similar to that of graphite, allowing more Si addition compared with the case of SiO_x. This characteristic is beneficial for the preparation of next-generation anode materials with higher energy densities. The adaptive design of composite anode materials containing various compositions and process combinations is expected to be useful to meet the requirements of advanced applications, such as long-range EVs that demand high energy densities. Therefore, we proposed a novel strategy for a practical Si/C composite anode with mechanical confinement and proved its commercial feasibility for replacement of conventional graphite anodes. As demonstrated in this study, improvements in the ICE and capacity retention by CVD treatment and composition optimization can contribute to the early commercialization of a Si/C composite anode for use in the battery industry. This could also be a significant breakthrough for the development of an EV with extended driving mileage that is several orders of magnitude greater than that available in current-generation, single-charge EVs.

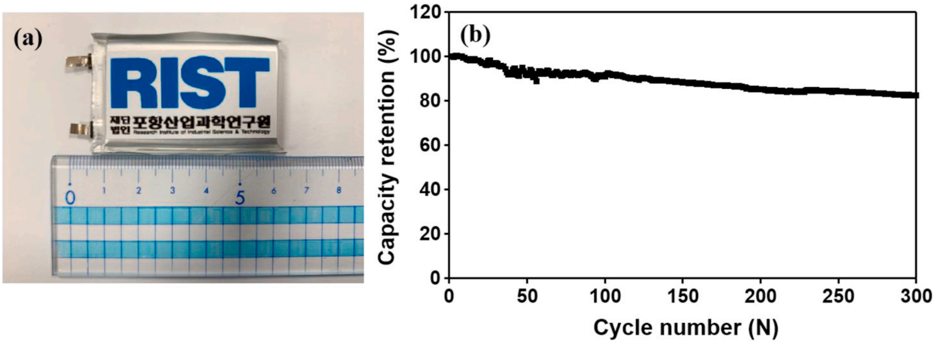

Fig. 8. (a) Photo and cell dimensions for battery packaging in a pouch-type full-cell configuration. The N/P ratio was 1.2. (b) Full-cell capacity retention for *m-C*-Si/C (10) paired with an NCM 622 cathode.

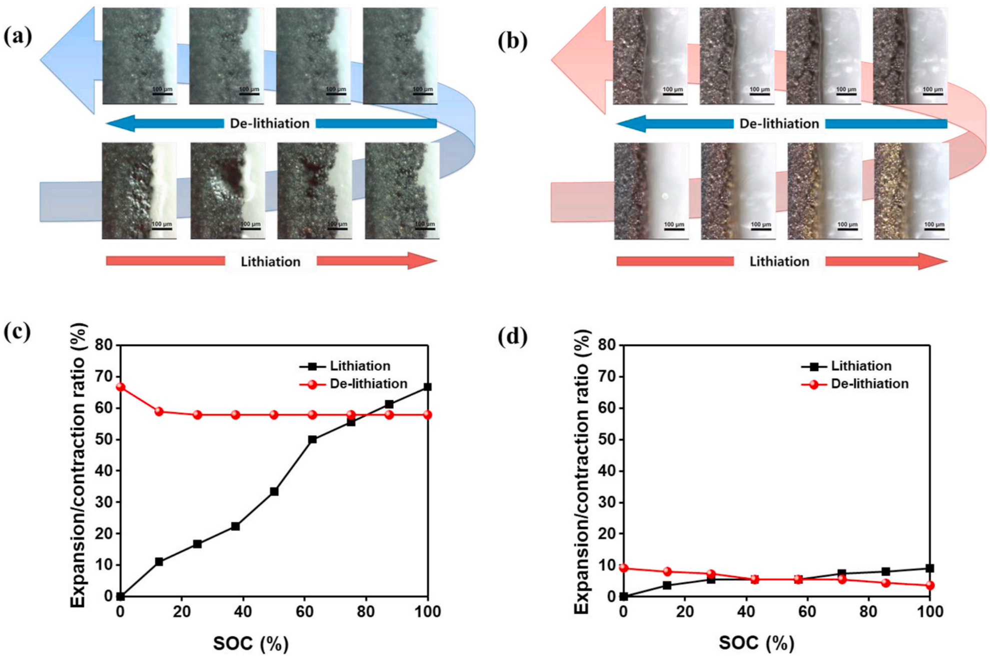

Fig. 9. Operando optical microscopy observations of anodes composed of micron-sized pure Si alone (a, c) and *C*–Si/C composite (b, d). Expansion and contraction ratios of both electrodes are shown in (c, d).

Declaration of competing interest

The authors declare that they have no known competing financial interests or personal relationships that could have appeared to influence the work reported in this paper.

Acknowledgements

The authors are grateful for the financial support of POSCO through the project based on LIB materials R&D. C.M.Y. acknowledges the financial support received from the Korea Institute of Science and Technology (KIST) Institutional Program and from the Nano Material Technology Development Program through the National Research Foundation of Korea (NRF) funded by the Ministry of Science and ICT (grant no. 2016M3A7B4027695).

Appendix A. Supplementary data

Supplementary data to this article can be found online at https://doi.org/10.1016/j.compositesb.2021.108799.

Author contributions

Moon Kyu Cho: Methodology, Investigation, Formal analysis. **Seung Jae You:** Methodology, Investigation, Formal analysis. **Jung Gyu Woo:** Methodology, Investigation, Formal analysis. **Jung-Chul An:** Formal analysis, Data curation. **Sujin Kang:** Formal analysis, Data curation. **Hyun-Wook Lee:** Formal analysis, Data curation. **Ji Hoon Kim:** Methodology, Investigation, Formal analysis. **Cheol-Min Yang:** Supervision, Conceptualization, Methodology, Resources, Writing – review & editing, Project administration, Funding acquisition. **Yong Jung Kim:** Supervision, Conceptualization, Methodology, Resources, Writing – original draft, Writing – review & editing, Project administration, Funding acquisition.

References

[1] Tarascon J-M, Armand M. Issues and challenges facing rechargeable lithium batteries. Nature 2001;414:359–67.

[2] Kang KS, Meng YS, Bréger J, Grey CP, Ceder G. Electrodes with high power and high capacity for rechargeable lithium batteries. Science 2006;311(5763):977–80.

[3] Thackeray MM, Wolverton C, Isaacs ED. Electrical energy storage for transportation-approaching the limits of, and going beyond, lithium-ion batteries. Energy Environ Sci 2012;5:7854–63.

[4] Xu Z-L, Liu X, Luo Y, Zhou L, Kim J-K. Nanosilicon anodes for high performance rechargeable batteries. Prog Mater Sci 2017;90:1–44.

[5] Boukamp BA, Lesh GC, Huggins RA. All-solid lithium electrodes with mixed-conductor matrix. J Electrochem Soc 1981;128:725–9.

[6] Hatchard TD, Dahn JR. In situ XRD and electrochemical study of the reaction of lithium with amorphous silicon. J Electrochem Soc 2004;151:A838–42.

[7] Obrovac MN, Christensen L. Structural changes in silicon anodes during lithium insertion/extraction. Electrochem Solid State Lett 2004;7:A93–6.

[8] Liu N, Wu H, McDowell MT, Yao Y, Wang CM, Cui Y. A yolk-shell design for stabilized and scalable Li-ion battery alloy anodes. Nano Lett 2012;12:3315–21.

[9] Lu Z, Liu N, Lee HW, Zhao J, Li WY, Li YZ, Cui Y. Nonfilling carbon coating of porous silicon micrometer-sized particles for high-performance lithium battery anodes. ACS Nano 2015;9(3):2540–7.

[10] Liu N, Lu Z, Zhao J, McDowell MT, Lee HW, Zhao WT, Cui Y. A pomegranate-inspired nanoscale design for large-volume-change lithium battery anodes. Nat Nanotechnol 2014;9:187–92.

[11] Wu H, Cui Y. Designing nanostructured Si anodes for high energy lithium ion batteries. Nano Today 2012;7(5):414–29.

[12] Magasinski A, Dixon P, Hertzberg B, Kvit A, Ayala J, Yushin G. High-performance lithium-ion anodes using a hierarchical bottom-up approach. Nat Mater 2010;9:353–8.

[13] Cho JP. Porous Si anode materials for lithium rechargeable batteries. J Mater Chem 2010;20:4009–14.

[14] Sakabe J, Ohta N, Ohnish T, Mitsuishi K, Takada K. Porous amorphous silicon film anodes for high-capacity and stable all-solid-state lithium batteries. Commun Chem 2018;1:24.

[15] Huang Y, Peng J, Luo J, Li W, Wu Z, Shi M, Li X, Li N, Chang B, Wang X. Spherical Gr/Si/GO/C composite as high-performance anode material for lithium-ion batteries. Energy Fuels 2020;34:7639–47.

[16] Peng J, Luo J, Li W, Zeng P, Wu Z, Wang Y, Li J, Shu H, Wang X. Insight into the performance of the mosoporous structure SiO_x nanoparticles anchored on carbon fibers as anode material of lithium-ion batteries. J Electroanal Chem 2021;880:114798.

[17] Wang Z, Fu Y, Zhang S, Yuan S, Amine K, Battaglia V, Liu G. Application of stabilized lithium metal powder (SLMP®) in graphite anode–a high efficient prelithiation method for lithium-ion batteries. J Power Sources 2014;260:57–61.

[18] Chen T, Wu J, Zhang Q, Su X. Recent advancement of SiO_x based anodes for lithium-ion batteries. J Power Sources 2017;363:126–44.

[19] Jung SC, Kim H-J, Kim J-H, Han Y-K. Atomic-level understanding toward a high-capacity and high-power silicon oxide (SiO) material. J Phys Chem 2016;120:886–92.

[20] Li Y, Yan K, Lee H-W, Lu Z, Liu N, Cui Y. Growth of conformal graphene cages on micrometre-sized silicon particles as stable battery anodes. Nat Energy 2016;1:15029.

[21] Yeom SJ, Lee CM, Kang SJ, Wi TU, Lee CH, Chae SJ, Cho JP, Shin DO, Ryu JK, Lee HW. Native void space for maximum volumetric capacity in silicon-based anodes. Nano Lett 2019;19:8793–800.

[22] Piper DM, Yersak TA, Lee SH. Effect of compressive stress on electrochemical performance of silicon anodes. J Electrochem Soc 2013;160:A77–81.

[23] Son SB, Kim SC, Kang CS, Yersak TA, Kim YC, Lee CG, Moon SH, Cho JS, Moon JT, Oh KH, Lee SH. A highly reversible nano-Si anode enabled by mechanical confinement in an electrochemically activated $Li_xTi_4Ni_4Si_7$ matrix. Adv Energy Mater 2012;2:1226–31.

[24] Whiteley JM, Kim JW, Piper DM, Lee SH. High-capacity and highly reversible silicon-tin hybrid anode for solid-state lithium-ion batteries. J Electrochem Soc 2016;163:A251–4.

[25] Dunlap NA, Kim SC, Jeong JJ, Oh KH, Lee SH. Simple and inexpensive coal-tar-pitch derived Si-C anode composite for all-solid-state Li-ion batteries. Solid State Ionics 2018;324:207–17.

[26] Saint J, Morcrette M, Larcher D, Laffont L, Beattie S, Pérès J-P, Talaga D, Couzi M, Tarascon J-M. Towards a fundamental understanding of the improved electrochemical performance of silicon-carbon composites. Adv Funct Mater 2007;17:1765–74.

[27] Liu Y, Wen ZY, Wang XY, Yang XL, Hirano A, Imanishi N, Takeda Y. Improvement of cycling stability of Si anode by mechanochemical reduction and carbon coating. J Power Sources 2009;189:480–4.

[28] Dimov N, Kugino S, Yoshio M. Carbon-coated silicon as anode material for lithium ion batteries: advantages and limitations. Electrochim Acta 2003;48:1579–87.

[29] Liu XH, Zhong L, Huang S, Mao SX, Zhu T, Huang JY. Size-dependent fracture of silicon nanoparticles during lithiation. ACS Nano 2012;6:1522–31.

[30] Yu BC, Hwa Y, Kim JH, Sohn HJ. Carbon coating for Si nanomaterials as high-capacity lithium battery electrodes. Electrochem Commun 2014;46:144–7.

[31] Han X, Chen HX, Zhang ZQ, Huang DL, Xu JF, Li C, Chen SY, Yang Y. Carbon-coated Si micrometer particles binding to reduced graphene oxide for a stable high-capacity lithium-ion battery anode. J Mater Chem 2016;4:17757–63.

[32] Lee JH, Kim W-J, Kim J-Y, Lim S-H, Lee S-M. Spherical silicon/graphite/carbon composites as anode material for lithium-ion batteries. J Power Sources 2008;176:353–8.

[33] Jo YN, Kim Y, Kim JS, Song JH, Kim KJ, Kwag CY, Lee DJ, Park CW, Kim YJ. Si-graphite composites as anode materials for lithium secondary batteries. J Power Sources 2010;195:6031–6.

[34] Chae SJ, Kim NH, Ma JY, Cho JP, Ko MS. Lithium-ion batteries: one-to-one comparison of graphite-blended negative electrodes using silicon nanolayer-embedded graphite versus commercial benchmarking materials for high-energy lithium-ion batteries. Adv Energy Mater 2017;7:1700071.

[35] Ko MS, Chae Sj, Ma JY, Kim NH, Lee HW, Cui Y, Cho JP. Scalable synthesis of silicon-nanolayer-embedded graphite for high-energy lithium-ion batteries. Nat Energy 2016;1:16113.

[36] Liu WR, Wang JH, Wu HC, Shieh DT, Yang MH, Wu NL. Electrochemical characterizations on Si and C-Coated Si particle electrodes for lithium-ion batteries. J Electrochem Soc 2005;152:A1719–25.

[37] Yen YC, Chao SC, Wu HC, Wu NL. Study on solid-electrolyte-interphase of Si and C-coated Si electrodes in lithium cells. J Electrochem Soc 2009;156:A95–102.

[38] Choi SH, Nam GT, Chae SJ, Kim DH, Kim NH, Kim WS, Ma JY, Sung JK, Han SM, Ko MS, Lee HW, Cho JP. Robust pitch on silicon nanolayer-embedded graphite for suppressing undesirable volume expansion. Adv Energy Mater 2018;9:1803121.

[39] Foss CEL, Svensson AM, Sunde S, Vullum-Bruer F. Edge/basal/defect ratios in graphite and their influence on the thermal stability of lithium ion batteries. J Power Sources 2016;317:177–83.

[40] Placke T, Siozios V, Schmitz R, Lux SF, Bieker P, Colle C, Meyer H-W, Passerini S, Winter M. Influence of graphite surface modifications on the ratio of basal plane to "non-basal plane" surface area and on the anode performance in lithium ion batteries. J Power Sources 2012;200:83–91.

[41] An JC, Lee EJ, Yoon S-Y, Lee SY, Kim YJ. Comparative study on the morphological properties of graphene nanoplatelets prepared by an oxidative and non-oxidative route. Carbon Lett 2018;26:1–7.